SAND2024-02269J

ARTICLE

Manganese-based A-site high-entropy perovskite oxide for solar thermochemical hydrogen production

Received 00th January 20xx,
Accepted 00th January 20xx

DOI: 10.1039/x0xx00000x

Cijie Liu,‡[a] Dawei Zhang,‡[b] Wei Li,*[a] Jamie A. Trindell,[c] Keith A. King,[c] Sean R. Bishop,[d] Joshua D. Sugar,[c] Anthony H. McDaniel,[c] Andrew I. Smith,[d] Perla A. Salinas,[d] Eric N. Coker,[d] Arielle L. Clauser,[c] Murugesan Velayutham,[ef] Joerg C. Neuefeind,[g] Jingjing Yang,[b] Héctor A. De Santiago,[a] Liang Ma,[a] Yi Wang,[a] Qiang Wang,[h] Wenyuan Li,[i] Qingsong Wang,[j] Qingyuan Li,[a] Hanchen Tian,[a] Ha Ngoc Ngan Tran,[i] Xuemei Li,[i] Brandon Robinson,[i] Angela M. Deibel,[a] Gregory Collins,[a] Nhat Anh Thieu,[a] Jianli Hu,[i] Valery V. Khramtsov,[ef] Jian Luo,*[bk] and Xingbo Liu*[a]

Non-stoichiometric perovskite oxides have been studied as a new family of redox oxides for solar thermochemical hydrogen (STCH) production owing to their favourable thermodynamic properties. However, conventional perovskite oxides suffer from limited phase stability and kinetic properties, and poor cyclability. Here, we report a strategy of introducing A-site multi-principal-component mixing to develop a high-entropy perovskite oxide, $(La_{1/6}Pr_{1/6}Nd_{1/6}Gd_{1/6}Sr_{1/6}Ba_{1/6})MnO_3$ (LPNGSB_Mn), which shows desirable thermodynamic and kinetics properties as well as excellent phase stability and cycling durability. LPNGSB_Mn exhibits enhanced hydrogen production (~77.5 mmol mol_{oxide}^{-1}) compared to $(La_{2/3}Sr_{1/3})MnO_3$ (~53.5 mmol mol_{oxide}^{-1}) in a short 1-hour redox duration and high STCH and phase stability for 50 cycles. LPNGSB_Mn possesses a moderate enthalpy of reduction (252.51-296.32 kJ $(mol\text{-}O)^{-1}$), a high entropy of reduction (126.95-168.85 J $(mol\text{-}O)^{-1}$ K^{-1}), and fast surface oxygen exchange kinetics. All A-site cations do not show observable valence changes during the reduction and oxidation processes. This research preliminarily explores the use of one A-site high-entropy perovskite oxide for STCH.

Introduction

Hydrogen fuels are promising, environmentally-friendly energy sources with high efficiency and renewability.[1-5] To realize large-scale hydrogen production and store intermittent solar energy, solar-driven thermochemical hydrogen (STCH) attracts considerable attention because it utilizes the full spectrum of solar energy through a two-step redox cycle.[6-10] (1) The first step of the process involves the reduction of metal oxide under high temperatures (e.g., $T > 1473$ K) and low P_{O_2} (partial pressure of oxygen), resulting in the production of oxygen vacancies. (2) The second step involves oxidizing the metal oxide with steam at low temperatures (e.g., $T < 1373$ K) to produce hydrogen.[11, 12]

$$\text{Reduction step: } A_nBO_3 \rightarrow A_nBO_{3-\delta} + \frac{\delta}{2}O_2 \quad (1)$$

$$H_2O \text{ splitting: } A_nBO_{3-\delta} + \delta H_2O(g) \rightarrow A_nBO_3 + \delta H_2(g) \quad (2)$$

[a] *Department of Mechanical and Aerospace Engineering, Benjamin M. Statler College of Engineering and Mineral Resources, West Virginia University, Morgantown, WV 26506, USA. E-mail: wei.li@mail.wvu.edu; xingbo.liu@mail.wvu.edu*
[b] *Program in Materials Science and Engineering, University of California San Diego, La Jolla, CA 92093, USA*
[c] *Sandia National Laboratories, Livermore, CA 94551, USA*
[d] *Sandia National Laboratories, Albuquerque, NM 87123, USA*
[e] *In Vivo Multifunctional Magnetic Resonance center, Robert C. Byrd Health Sciences Center, West Virginia University, Morgantown, WV 26506, USA*
[f] *Department of Biochemistry and Molecular Medicine, School of Medicine, West Virginia University, Morgantown, WV 26506, USA*
[g] *Chemical and Engineering Materials Division, Oak Ridge National Laboratory, Oak Ridge, TN 37831, USA*
[h] *Shared Research Facilities, West Virginia University, Morgantown, WV 26506, USA*
[i] *Department of Chemical and Biomedical Engineering, Benjamin M. Statler College of Engineering and Mineral Resources, West Virginia University, Morgantown, WV 26506, USA*
[j] *Bavarian Center for Battery Technology (BayBatt), Department of Chemistry, University of Bayreuth, Universitätsstrasse 30, 95447 Bayreuth, Germany*
[k] *Department of Nano and Chemical Engineering, University of California San Diego, La Jolla, CA 92093, USA. E-mail: jluo@alum.mit.edu*
‡These authors (C.L. and D.Z.) contributed equally to this work.
*Corresponding authors
Electronic Supplementary Information (ESI) available.

The active redox metal oxides that have been investigated for STCH include stoichiometric oxides (e.g., SnO_2/SnO[13] and ZnO/Zn[14]) and non-stoichiometric oxides (e.g., ceria and perovskite-type oxide). Stoichiometric oxides usually require high reduction temperatures (≥1873 K) to reduce, and the reduction-oxidation rates are low.[15] Additionally, the reduced oxide is in the gas phase, which increases the collection and separation cost. Ceria ($CeO_{2-\delta}$, where δ represents oxygen non-stoichiometry) materials are well-investigated for STCH reactions due to their thermal stability and fast reaction kinetics. However, ceria suffers from high reduction temperatures (1823 K or above), limiting the theoretical hydrogen yield.[16-19] Perovskite-type oxide materials ($ABO_{3-\delta}$) are considered a promising candidate for STCH reaction because they have a low standard partial molar reduction enthalpy resulting in high Δδ. Additionally, the Δδ value of perovskite can be tuned to achieve desirable thermodynamic and kinetic properties, which have been widely studied.[20-23] For instance, the Δδ value of the perovskite family $La_xSr_{1-x}Mn_yAl_{1-y}O_{3-\delta}$ ($0\le x\le 1$, $0\le y\le 1$) is tuneable and increases with the increasing of Sr concentration.[24] However, the issue of phase instability and poor cycling performance, as well as sintering and slow kinetics in the reduction step, remains a challenge. For instance, La and, Gd dopants in $BaFeO_{3-\delta}$ have been investigated in STCH, but they suffer from the problem of phase instability after the thermochemical H_2O splitting reaction. Notably, the poor cycling stability of La- and Gd-doped $BaFeO_{3-\delta}$ system also limits the potential for development in STCH. Additionally, the time required for one redox cycle is usually longer than 1.5 hours, which is unfavourable for energy utilization. Therefore, searching for materials with desirable phase stability and kinetics during short-time redox cycling reactions is important.

High-entropy ceramics (HECs) include a wide number of materials such as high-entropy oxides, borides, carbides, silicides, sulfides, phosphides, and phosphates.[25-28] Specifically, high-entropy perovskite oxides (HEPOs) were reported in 2018,[29] and subsequently attracted great interest because of their catalytic, dielectric, ferroelectric, magnetic, thermoelectric, magnetocaloric, & electrocaloric properties, as well as promising applications in solid oxide fuel cells, batteries, and supercapacitors.[30-33] Recent studies found high-entropy oxides with favourable kinetics and stability in the cycling redox reaction.[34-38] For example, the $(FeMgCoNi)O_{1.2}$@SiC composite demonstrated a hydrogen yield that surpassed the thermodynamic limits of cutting-edge materials, including spinel ferrites and ceria.[39] Also, $(FeMgCoNi)O_{1.2}$ showed no performance degradation for 10 cycles. Recently, HECs have been further extended to compositionally complex ceramics (CCCs) where maximizing the configurational entropy is not always needed or beneficial.[28, 40] Notably, a recent report showed that compositionally complex perovskite oxides (CCPOs) with non-equimolar B-site mixing exhibit excellent STCH performance with Co as the redox-active element.[41]

Herein, we reported a Mn-based HEPO for STCH reaction via A-site mixing with the chemical formula $(La_{1/6}Pr_{1/6}Nd_{1/6}Gd_{1/6}Sr_{1/6}Ba_{1/6}Mn)O_3$, denoted as LPNGSB_Mn for brevity, for STCH reaction with further improved performance (and are Co-free). LPNGSB_Mn possesses excellent phase stability even after 50 cycling reactions. LPNGSB_Mn exhibits a favourable kinetic property (oxygen exchange coefficient), desirable thermodynamic parameters (Δδ, enthalpy, and entropy of reduction), and high H_2 production (~77.5 mmol mol_{oxide}^{-1}) within 1 h. The conclusion that Mn is the only redox centre in this material is supported by X-ray photoelectron spectroscopy (XPS) and electron energy loss spectroscopy (EELS) results. Moreover, LPNGSB_Mn shows excellent phase stability and cycling durability even after over 50 long cycles. This work also provides a new pathway for utilizing A-site HEPO in thermochemical applications such as chemical looping and explores the potential of HEPOs for use in two-step seawater splitting. In this study, we explore both kinetic and thermodynamic aspects in a high-entropy system. Additionally, our extended testing over 50 cycles indicates long-term stability and potential for application, thereby enriching the current understanding beyond the state-of-the-art redox oxides in this field.[39, 42, 43]

Results and discussion

2.1 Characterizations and Experiments

The nominal compositions and sample abbreviations for perovskite oxides developed in this work are shown in **Table 1**.

Table 1. Compositions of developed perovskite oxides and sample abbreviations.

Sample abbreviations	Nominal composition
LS21_Mn	$(La_{2/3}Sr_{1/3})MnO_3$
LPNGSB_Mn	$(La_{1/6}Pr_{1/6}Nd_{1/6}Gd_{1/6}Sr_{1/6}Ba_{1/6})MnO_3$

X-ray diffraction (XRD) patterns revealed that samples exhibited rhombohedral crystal structures (with space group $R\bar{3}c$) without any detectable secondary phase (**Figure 1**a). Rietveld refinements confirm all compositions are $R\bar{3}c$ phase by assuming random A site occupation of La, Pr, Nd, Gd, Sr, and Ba (**Figure S1, S2**). **Table S1** displays the refined lattice parameters for samples. In addition, the neutron total scattering conducted at Oak Ridge National Laboratory (ORNL) Spallation Neutron Source (SNS) Nanoscale-Ordered Materials Diffractometer (NOMAD) further confirmed that LS21_Mn has a rhombohedral crystal structure, as shown in **Figure S3**. The fitting results of the NOMAD data are presented in **Table S2**. The comparison between the XRD and NOMAD neutron total scattering results shows excellent agreement, which further validates the

crystal structure and space group. The crystal structure is shown in **Figure 1**b. Additionally, the tolerance factor of LPNGSB_Mn can be calculated by Eq. (3).

$$\tau = \frac{r_A + r_o}{\sqrt{2}(r_B + r_o)} \quad (3)$$

Here, r_A, r_o, and r_B represent the ionic radii of each ion. The τ of LPNGSB_Mn is 0.9925. Generally, when $0.89 < \tau < 1.02$, the perovskite structure is stable.[44]

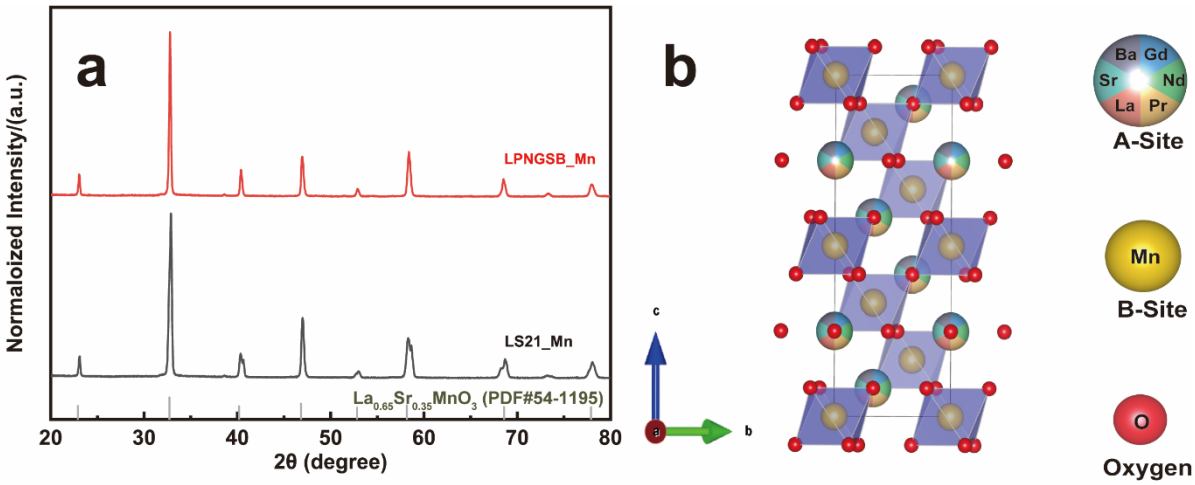

Figure 1 (a) XRD patterns of LPNGSB_Mn and LS21_Mn. The standard XRD card for $La_{0.65}Sr_{0.35}MnO_3$ with structure is shown for reference. (b) Crystal Structure of LPNGSB_Mn.

The morphologies, microstructure, and elemental distribution of LPNGSB_Mn were characterized using scanning electron microscopy (SEM) in combination with energy-dispersive X-ray (EDX) spectroscopy (**Figure 2**). The fresh sample showed irregularly connected spherical particles with an average diameter of approximately 5-15 µm. The EDX mappings showed a homogeneous distribution of elements.

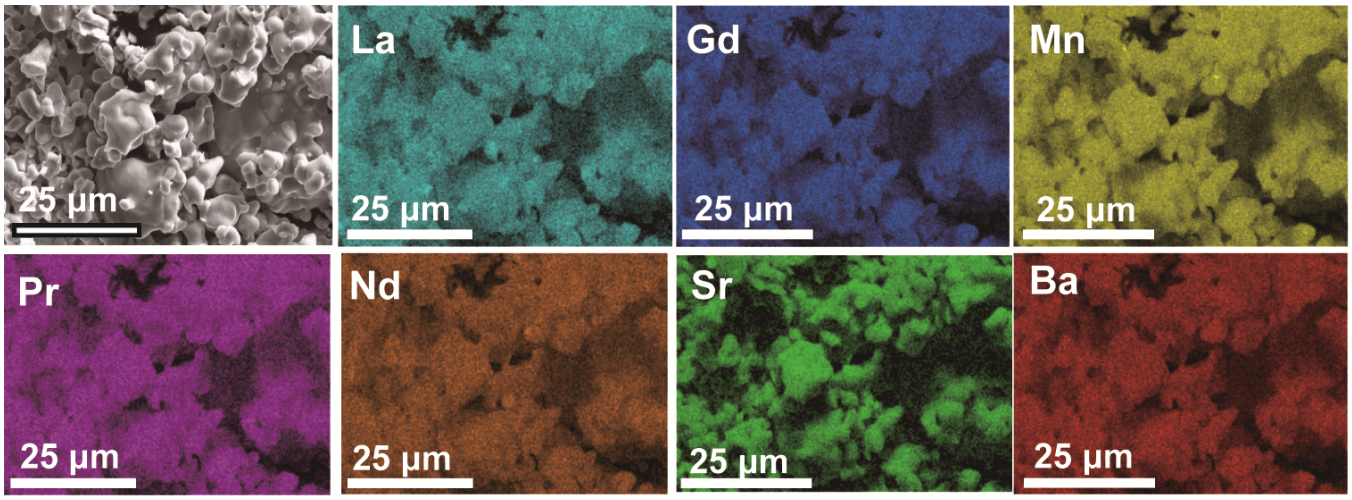

Figure 2 SEM images and corresponding EDX elemental maps showing the distribution of La (cyan), Pr (purple), Nd (orange), Gd (blue), Sr (green), Ba (red), and Mn (yellow) in the fresh $(La_{1/6}Pr_{1/6}Nd_{1/6}Gd_{1/6}Sr_{1/6}Ba_{1/6})MnO_3$ (LPNGSB_Mn) perovskite sample.

The scanning transmission electron microscopy (STEM) with EDX mapping (**Figure 3**) was used to characterize the atomic microstructure and elemental distribution of LPNGSB_Mn, which revealed a uniform distribution of all elements. These results show a homogenous occupancy of A sites between the A site dopants, but that B-sites are occupied by Mn. STEM-EDX quantitative analysis displayed the average composition for all metal percentages as shown in **Table S3**.

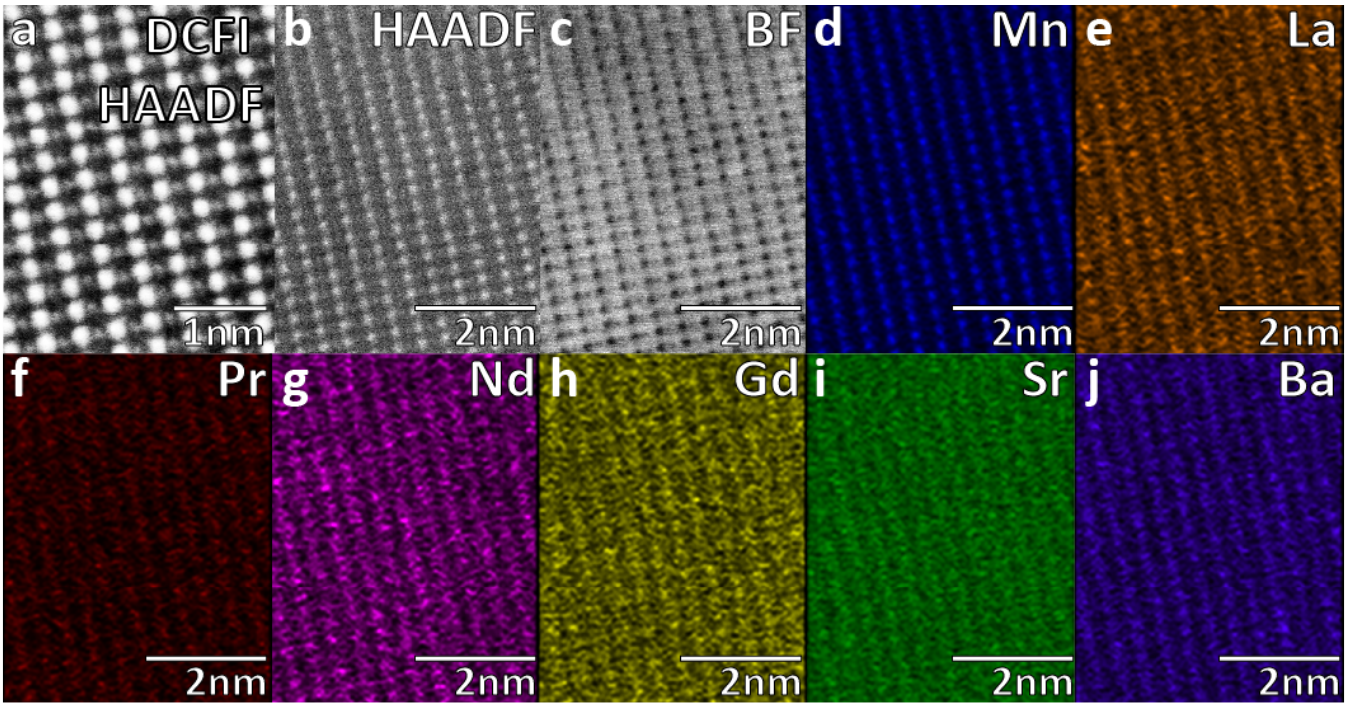

Figure 3 Pristine LPNGSB_Mn (a) drift corrected frame integrated (DCFI) HAADF image showing A and B-site atoms as white and gray points of contrast respectively. (b) HAADF image (c) bright-field (BF) image (d) well-ordered Mn EDX map corresponding to the gray points of contrast in the HAADF image. (e) La EDX map (f) Pr EDX map (g) Nd EDX map (h) Gd EDX map (i) Sr EDX map and (j) Ba EDX map. (e-j) show atomic signals corresponding to the brightest white points in the HAADF images indicating a mixed species A-site occupation.

To assess the redox capability, the LPNGSB_Mn series samples were tested by temperature programmed reduction (TPR).[45] **Figure S4** displays that LPNGSB_Mn has a larger Δδ than LS21_Mn. LPNGSB_Mn shows a Δδ value of 0.0822, which is approximately 2.6 times greater than that of LS21_Mn (Δδ = 0.032).

EPR technique was used to study the magnetic properties of perovskite oxides. The formation of oxygen vacancy in LPNGSB_Mn was investigated using EPR spectroscopy. Room temperature X-band EPR spectra were recorded for the powder samples of fresh LPNGSB_Mn and reduced LPNGSB_Mn (thermally reduced at 1350 °C under nitrogen atmosphere). EPR spectra of fresh LPNGSB_Mn and reduced LPNGSB_Mn samples are shown in **Figure S5**. Both fresh LPNGSB_Mn and reduced LPNGSB_Mn samples exhibited a broad and symmetric signal of high-spin Mn^{4+} (t_{2g}^3 e_g^0, S = 3/2) located in the cubic symmetry of the perovskite B site.[46-48] The broad spectrum is due to isotropic ferromagnetic exchange coupling arises from the hopping of electrons between Mn^{4+} and nearest neighbour Mn^{3+} ions in the crystal lattice.[48-50] The calculated g value for both spectra is g = 1.98. No EPR signal was observed below 2000 G (data not shown). The linewidth (ΔH_{pp}) values of fresh LPNGSB_Mn and reduced LPNGSB_Mn samples, calculated from the maximum and minimum values of the spectrum, were 704 and 680 G, respectively. As compared to the ΔH_{pp} of fresh LPNGSB_Mn, the ΔH_{pp} value of and reduced LPNGSB_Mn sample was significantly decreased (from 704 G to 680 G). EPR spectroscopy has been used to study the oxygen vacancy defects in the perovskite oxides.[47, 48, 51] Under a high external thermal energy, some oxygen ions deviated from the original sites and oxygen vacancies are generated in perovskite oxides. The increased sites of oxygen vacancies increase the electron concentration inside the crystals. Our EPR study shows that the g (= 1.98) value of the reduced LPNGSB_Mn sample is same as the fresh LPNGSB_Mn. It shows that the lattice structure and coordination environment of Mn^{4+} in LPNGSB_Mn sample is not changed even after heated at 1350 °C under nitrogen atmosphere. The formation of oxygen vacancies results in defect induced free electron spins. EPR studies have shown that the electrons trapped in the formation of oxygen vacancy sites exhibits a sharp signal around g = 2.003 - 2.004.[52, 53] In our study, due to the broad EPR spectra that lack any resolved fine structure, the characteristic g-value of oxygen vacancy cannot be extracted from the spectrum. Importantly, the change in ΔH_{pp} is attributed to the changes of magnetic interaction between

the Mn^{4+} and newly formed oxygen vacancies in reduced LPNGSB_Mn sample. The decreased ΔH_{pp} in reduced LPNGSB_Mn sample demonstrates that there is an increased exchange/magnetic interaction between Mn^{4+} and neighbouring electrons with the free spins induced by the oxygen vacancies. Overall, the EPR study clearly demonstrates that LPNGSB_Mn under external thermal energy and nitrogen atmosphere resulted in oxygen vacancies.

To reveal the redox-active elements in LPNGSB_Mn, in-situ electron energy loss spectroscopy (EELS) was conducted to investigate their redox activity by heating LPNGSB_Mn to 700 °C under a vacuum (**Figure S6**). The EELS spectra of Mn, O, La, Pr, Nd, Gd, and Ba are shown in **Figure S6**a-g. For the A-site elements, no cation peak shift was observed, indicating no valence change in the A-site elements.[41] For the B-site elements, Mn is the only redox-active element, as evidenced by the shift in the Mn L-edge to lower energies (**Figure S6**a). The XPS analysis of LPNGSB_Mn shows the same trend, with a shift in the peak edge to lower energies, further demonstrating that Mn is the redox-active element (**Figure S6**h). The Mn2p peak has two split spin-orbit components of 2p3/2 (~642.3 eV) and 2p1/2 (~653.5 eV). The differences in the binding energy of split (ΔBE) were 11.2 eV in fresh LPNGSB_Mn and increased to 11.7 eV in reduced LPNGSB_Mn. The results show a shift of the Mn 2p3/2 and Mn2p1/2 peaks toward lower binding energies, indicating that Mn has been reduced.[54] The absence of the satellite peak at 648 eV indicates that Mn^{2+} does not dominate in this oxide.[55] Thus, Mn^{3+}, and Mn^{4+} are the predominant valence states in this perovskite-type oxide.

The XPS results also confirmed that rare earth elements (La, Pr, Nd, Gd) remained stable without any change in LPNGSB_Mn before and after the reduction process (**Figure S7** and, **S8**). One observable change, shown in **Fig. S8**e, is that the Sr signal increases in intensity after reduction at 1350 °C. This change in Sr signal can be attributed to Sr segregation, which is commonly observed in perovskite oxides like $LaSrMnO_3$ series.[56, 57]

Note that direct water thermolysis catalysed by the samples and an alumina tube at 1100 °C produces a small amount of H_2, which is also reported in the literature.[58-62] The H_2 production from direct water thermolysis was measured at 800-1100 °C (**Figure S9**). Thus, the amount of hydrogen background produced through direct thermolysis was subtracted from the total hydrogen production to obtain the net H_2 production from the STCH redox reaction. To evaluate the water-splitting capabilities of LPNGSB_Mn and LS21_Mn in terms of hydrogen production and reversibility, these materials were subjected to consecutive H_2O-splitting cycles. **Figure 4**a shows the cumulative hydrogen production for both samples under different protocols in terms of different oxidation temperatures and reduction/oxidation durations at different cycles. **Figure 4**b presents the corresponding oxygen production under these protocols. The protocols implemented are detailed in **Table S4**. For all materials under different protocols, the molar ratio of O_2 to H_2 produced in the reduction and oxidation step respectively, was approximately 0.5 (**Figures S10** and **S11**), indicating that the splitting of H_2O is realized by the redox reaction in a stepwise way. As shown in **Figure 4**a and **Table 2**, hydrogen production increases with the number of cycles. Notably, LPNGSB_Mn exhibits the highest H_2 production (~77.5 mmol mol_{oxide}^{-1}) at 900 °C in the oxidation step. The H_2 production of LPNGSB_Mn is comparable with the reported oxides tested by the same reactor at Sandia National Laboratories, as shown in **Table S5**.[63, 64]

Initially, the hydrogen production of LS21_Mn (~26.7 mmol mol_{oxide}^{-1}) and LPNGSB_Mn (~26.3 mmol mol_{oxide}^{-1}) is similar when both thermally are reduced for 5 min (Protocol P1). However, the reduction and oxidation time increases, the hydrogen production of LPNGSB_Mn and LS21_Mn is 57 and 43.35 mmol mol_{oxide}^{-1} under Protocol P2, respectively. In a comparison between conditions of Protocols P2 and P3, with the reduction temperature fixed at 1350 °C, the oxidation temperatures are set at 1100 and 900 °C, respectively. A lower oxidation temperature of 900 °C is favourable, yielding a hydrogen production of ~73 mmol mol_{oxide}^{-1} for LPNGSB_Mn and ~53.5 mmol mol_{oxide}^{-1} for LS21_Mn, respectively, as shown in **Figure 4**a. The hydrogen production of LPNGSB_Mn in the 4th cycle at 900 °C (~77.5 mmol mol_{oxide}^{-1}) is higher than 1100 °C (~60 mmol mol_{oxide}^{-1}), suggesting a greater extent of the reaction at 900 °C, indicating a more thermodynamically favourable condition compared to 1100 °C. The oxidation reaction kinetics are favoured at higher temperatures, as shown in the plots of molar hydrogen production rate versus time (**Figure 4**c-h). The oxidative water splitting step is an exothermic reaction and thus thermodynamically favoured at a lower temperature. In contrast, the H_2 production kinetics at 1100 °C are higher than at 900 °C, as indicated by the higher peak rates at 1100 °C. The detailed values can be found in **Table S6**. The favoured thermodynamics at 900 °C likely cause the higher H_2 production within 30 min. A similar effect of lower oxidation temperature on the increased H_2 production has been reported in $La_{0.6}Ca_{0.4}MnO_3$.[65]

Figure 4i,j shows the rate curve for LPNGSB_Mn during high-conversion water-splitting cycles (with a molar ratio of H_2O to H_2 at 1000:1) at temperatures of 1100 and 900 °C with detailed conditions described in **Table S4**. The plots of gas molar production rates versus time for high conversion water-splitting cycles are shown in **Figure S12**. LPNGSB_Mn exhibits similar peak rates in the presence of H_2 at 1100 and 900 °C, as shown in **Figure 4**i,j. **Figure S13** compares LS21_Mn and LPNGSB_Mn in high-conversion water-splitting cycles, where LPNGSB_Mn shows a higher H_2 production peak rate than LS21_Mn. Moreover, hydrogen production can be detected in LPNGSB_Mn at 900 °C under Protocol P5, while LS21_Mn shows negligible H_2 production under the same conditions. After STCH cycles, the sample of LPNGSB_Mn was kept as the reduced state and characterized by the HAADF-STEM. The atomic-level crystal structure of reduced LPNGSB_Mn remains intact, and the distribution of elements is homogenous (**Figure S14**), indicating its phase stability. The STEM-EDX quantitative analysis of reduced LPNGSB_Mn is shown in **Table S7**.

In addition, it delivers similar H_2 production under the seawater vapor feeding condition. Therefore, this STCH technology can flexibly

function for splitting low-grade water without the reliance on the costly deionized water due to the use of H_2O vapor feeding, which is a promising technological complement to proton exchange membrane and anion exchange membrane water electrolysis that need to use deionized water.[66-71] Furthermore, the surface oxygen exchange kinetics for a dense LPNGSB_Mn pellet (**Figure S15**) were measured by the electrical conductivity relaxation (ECR) method. The ECR result (**Figure S16**) can be fitted to obtain the surface oxygen exchange coefficient (K_s).[72, 73] The K_s of LPNGSB_Mn is 7.992×10^{-5} cm s^{-1}.

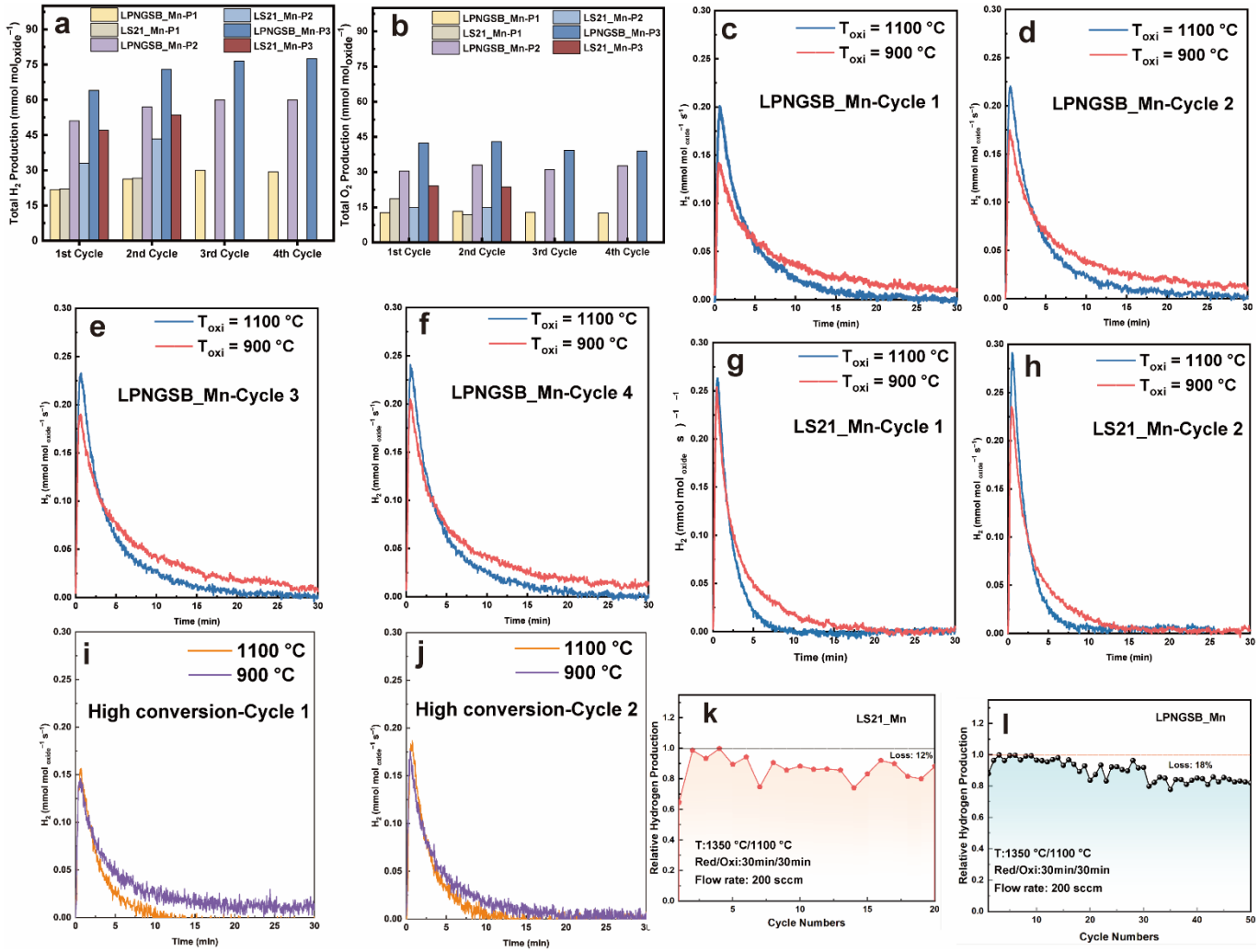

Figure 4 H_2 (a) and O_2 (b) production for LS21_Mn and LPNGSB_Mn under different protocols and cycles, respectively. The plots of molar H_2 production rate versus time for LPNGSB_Mn under protocols P2 and P3 in different cycles (c-f). The plots of molar H_2 production rate versus time for LS21_Mn under protocols P2 and P3 in different cycles (g-h). The plots of molar H_2 production rate versus time for LPNGSB_Mn under protocols P4 and P5 in different cycles (i-j). Cycling stability of H_2 production of LPNGSB_Mn (k) and LS21_Mn (l) under Protocol P2. Detailed testing protocols are summarized in Table S4. Results of (a-j) were obtained in a STCH reactor at Sandia National Laboratories, while results of k and l were obtained in another homemade reactor.

Table 2. Summary of STCH Production Results of LPNGSB_Mn under Different Testing Conditions.[a]

Condition	T_{red}/ T_{ox} (°C)	t_{red}/ t_{ox} (min)	Flow rate (sccm)	Cumulative H_2 production (mmol mol_{oxide}^{-1})	Steam to hydrogen conversion (%)
C1-LPNGSB_Mn-P1	1350/1100	5/20	200	21.8	0.45

C2-LPNGSB_Mn-P1	1350/1100	5/20	200	26.3	0.54
C3-LPNGSB_Mn-P1	1350/1100	5/20	200	30	0.61
C4-LPNGSB_Mn-P1	1350/1100	5/20	200	29.3	0.60
C1-LS21_Mn-P1	1350/1100	5/20	200	22	0.55
C2-LS21_Mn-P1	1350/1100	5/20	200	26.7	0.67
C1-LPNGSB_Mn-P2	1350/1100	30/30	200	51	0.70
C2-LPNGSB_Mn-P2	1350/1100	30/30	200	57	0.78
C3-LPNGSB_Mn-P2	1350/1100	30/30	200	60	0.82
C4-LPNGSB_Mn-P2	1350/1100	30/30	200	60	0.82
C1-LS21_Mn-P2	1350/1100	30/30	200	32.95	0.55
C2-LS21_Mn-P2	1350/1100	30/30	200	43.35	0.71
C1-LPNGSB_Mn-P3	1350/900	30/30	200	64	0.87
C2-LPNGSB_Mn-P3	1350/900	30/30	200	73	1.0
C3-LPNGSB_Mn-P3	1350/900	30/30	200	76.5	1.05
C4-LPNGSB_Mn-P3	1350/900	30/30	200	77.5	1.05
C1-LS21_Mn-P3	1350/900	30/30	200	47	0.78
C2-LS21_Mn-P3	1350/900	30/30	200	53.5	0.89
C2-LPNGSB_Mn-P4	1350/1100	30/30	200	27.9-51	-
C2- LS21_Mn-P4	1350/1100	30/30	200	34.15-46.1	-
C2-LPNGSB_Mn-P5	1350/900	30/30	200	33.6-41.95	-

[a] In all cases, the cycle numbers are designated as C1 to C4. For example, C1 represents the first cycle. The protocol numbers are designed as P1 to P5 indicating different conditions which are detailed in Table S4. T_{red} and T_{ox} are the reduction and oxidation temperature, respectively. t_{red} and t_{ox} are the reduction and oxidation time, respectively.

Table 2 summarizes the STCH production results under different conditions/protocols. To investigate the correlation between H_2 production and material properties, we used excess steam to react with a small quantity of perovskite oxide samples to ensure the sufficient solid-gas contact and mass transfer for analysing the thermodynamic limit situation. Therefore, the steam-to-H2 conversion percentages under all conditions are lower than 1.1%.

We investigated the cycling ability of LS21_Mn for 20 cycles and LPNGSB_Mn for 50 cycles. **Figure 4**k,l shows the cycling test results. LPNGSB_Mn and LS21_Mn maintained stable hydrogen production, respectively. The cycling stability of LPNGSB_Mn under harsh cycling conditions is comparable to that reported for other STCH oxides.[92] LS21_Mn exhibits a degradation of 12% after 20 cycles. In contrast, LPNGSB_Mn shows a degradation of 18% after 50 cycles. The gradually decreased hydrogen production may be attributed to the particle coarsening of samples, which may decrease both the heat transfer rate and the oxygen release rate. The morphologies and EDX maps of pristine LPNGSB_Mn and LPNGSB_Mn cycled for 50 cycles are shown in **Figures 2**, **S17**, **S18**, and **S19**. After 50 cycles, LPNGSB_Mn had an average diameter of approximately 10-25 μm and did not show obvious element segregation. Regarding the texture of the samples, there was a considerable difference in the structural variation. The fresh LPNGSB_Mn sample had a rough surface with particle dispersion (**Figure 2**), compared to the 50-cycled sample, which had a relatively smoother surface (**Figure S17**d) with some particle aggregation and material sintering. The larger grain-size observed after the 50-cycling experiment could be attributed to the LPNGSB_Mn being exposed to high temperatures (1100-1350 °C) for a longer time. The distribution of different elements was analysed (**Figure 2** and **Figure S18, S19**). The elements of La, Pr, Nd, Gd, and Mn were distributed evenly in both the pristine and cycled LPNGSB_Mn, while the elements of Ba and Sr displayed small segregation in the cycled LPNGSB_Mn. This small difference can be attributed to the sample being subjected to high-temperature sintering. Therefore, the negligible element aggregations are consistent with the phase stability observed in the XRD pattern (**Figure S20**). This phenomenon commonly occurs in perovskite oxides containing alkaline earth elements like Sr, which have a significant influence on material activity and stability.[57]

The pristine and 50-cycled LPNGSB_Mn was characterized by Raman spectroscopy. The Raman spectra are shown in **Figure S21**, and a three-peak model was used to fit the spectra. The fitting results were summarized in **Table 3** below:

Table 3. The fitting result of the Raman spectroscopy peaks.

sample	Peak 1 (cm^{-1})	Peak 2 (cm^{-1})	Peak 3 (cm^{-1})
LPNGSB_Mn pristine	218	497	620
LPNGSB_Mn cycled	207	490	613

The observed vibrational band close to 600 cm^{-1} is probably due to Mn-O vibrational modes coupled with the MnO_6 octahedral structure, which are associated with the existence of oxygen vacancies nearby.[74, 75] The small peak shift between two samples could be attributed to the variation in the heavy ion content. The peaks close to 200 cm^{-1} and 490 cm^{-1} could be attributed to the A_{1g} mode from La vibration and the E_g mode from oxygen bending vibration, respectively. The peak around 620 cm^{-1} can be assigned to the B_{2g} mode, representing the in-phase stretching of LPNGSB_Mn.[76-79]

The structural stability of LPNGSB_Mn was further demonstrated based on the result of Raman.[77] Additionally, the red-shift is observed in the Raman spectra of 50-cycled LPNGSB_Mn indicating the increasing defects in the material structure.[80] Collectively, the results of XRD, SEM, EDX and Raman spectra indicate LPNGSB_Mn maintained the relatively stable composition, structure and phase.

Two thermodynamic properties, reduction enthalpy and entropy, are key factors that determine the H_2 production of STCH materials.[81, 82] Therefore, we measured the δ over a range of P_{O_2} values and temperatures for LS21_Mn and LPNGSB_Mn through a reported TGA method.[83-85] **Figure 5**a,b show the oxygen non-stoichiometry of LPNGSB_Mn and LS21_Mn, respectively, as a function of temperatures at different oxygen partial pressures P_{O_2}.

According to the van't Hoff method,[84] the standard entropy change (ΔS_O^o) and the standard enthalpy change (ΔH_O^o) can be acquired from the correlation with P_{O_2} and temperature as the following equation.[83, 85, 86]

$$\Delta G^{\circ}(T) = -RT\ln K_{red}^{eq} \quad (4)$$

$$\Delta G^{\circ}(T) = \Delta H_{red}^{\circ}(\delta) - T\Delta S_{red}^{\circ}(\delta) \quad (5)$$

$$K_{red}^{eq} = P_{O_2}^{\frac{1}{2}}(\delta) \quad (6)$$

$$\ln P_{O_2}^{\frac{1}{2}}(\delta) = -\frac{\Delta H_{red}^{\circ}(\delta)}{R}T^{-1} + \frac{\Delta S_{red}^{\circ}(\delta)}{R} \quad (7)$$

where $\Delta G^{\circ}(T)$ is Gibbs free energy in the temperature in Kelvin, K_{red}^{eq} is the thermodynamic equilibrium of reduction, $\Delta H_{red}^{\circ}(\delta)$ and $\Delta S_{red}^{\circ}(\delta)$ are the standard enthalpy and entropy, respectively, assuming $\Delta H_{red}^{\circ}(\delta)$ and $\Delta S_{red}^{\circ}(\delta)$ are irrelevant with temperature.

An Arrhenius plot of $\ln P_{O_2}^{\frac{1}{2}}$ vs 1000/*T* (at a specific δ) with linear fitting can be acquired. **Figure 5**c, d show the plots for LPNGSB_Mn and LS21_Mn, respectively. The value of $\Delta H_{red}^{\circ}(\delta)$ and $\Delta S_{red}^{\circ}(\delta)$ can be obtained from the slope and the intercept of the straight line, respectively. Consequently, the enthalpy and entropy of LS21_Mn and LPNGSB_Mn as a function of oxygen non-stoichiometry are obtained (**Figure 5**e, f), respectively and compared with those of some reported redox materials such as

ARTICLE

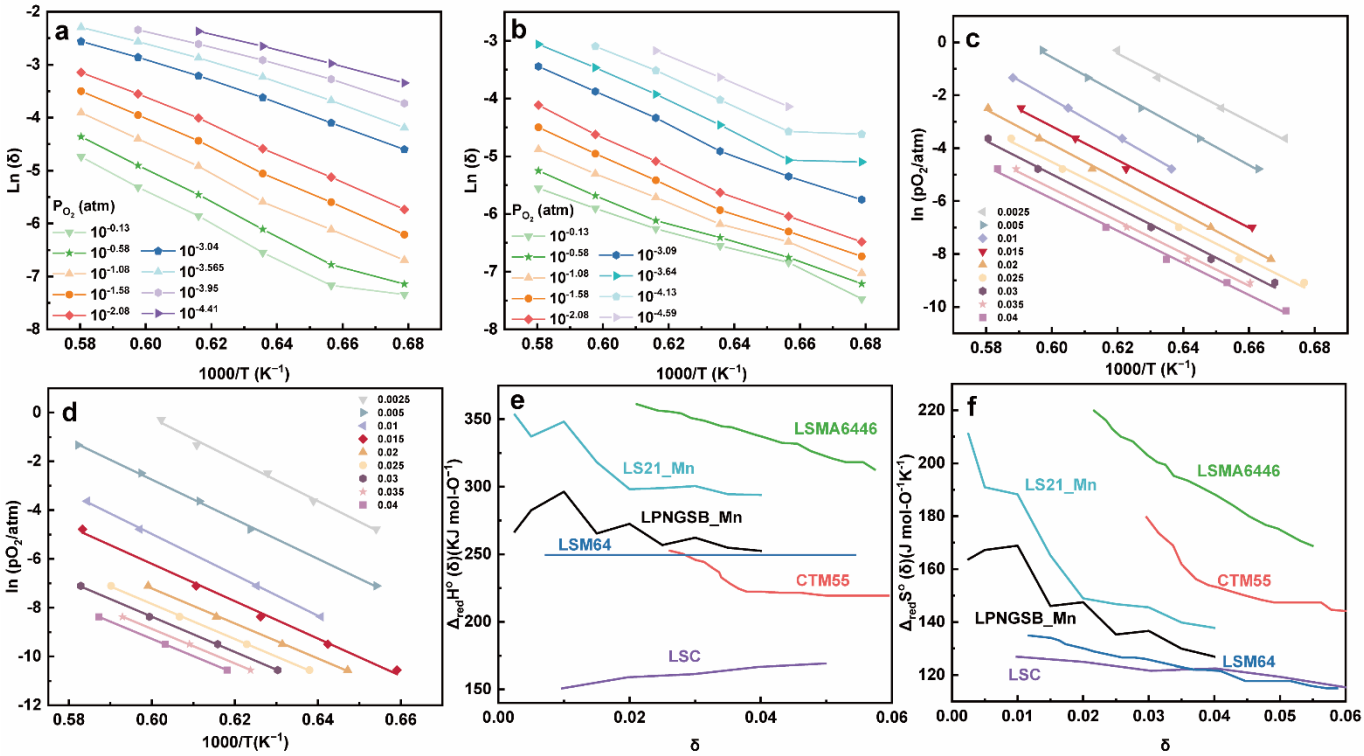

Figure 5 Oxygen non-stoichiometry of (a) LPNGSB_Mn and, (b) LS21_Mn as a function of temperatures at different oxygen partial pressures P_{O_2}. Arrhenius representation of (c) LPNGSB_Mn and (d) LS21_Mn in 1000/*T* and ln (P_{O_2}) for obtaining reduction enthalpy and entropy by the van't Hoff method at specific δ range from 0.0025-0.04. (e) Standard enthalpy and (f) entropy for LS21_Mn, LPNGSB_Mn, and some redox oxide materials reported in literatures (e.g., CTM55[19], LSMA6446[24], LSC[86] ,and LSM64[87]). The oxygen non-stoichiometry of (a) LPNGSB_Mn measured at 1400 °C was reprinted with permission from ref. [88]. Copyright 2023 The Electrochemical Society.

$La_{0.8}Sr_{0.2}CoO_3$ (LSC)[86], $Ca(Mn_{0.5}Ti_{0.5})O_{3-\delta}$ (CTM55), $La_{0.6}Sr_{0.4}MnO_{3-\delta}$ (LSM64)[87], $La_{0.6}Sr_{0.4}Mn_{0.4}Al_{0.6}O_{3-\delta}$ (LSMA6446).[24] LPNGSB_Mn is in a favourable window of $\Delta H^{\circ}_{red}(\delta)$ and $\Delta S^{\circ}_{red}(\delta)$. The reduction enthalpy and entropy of reduction are in the range of 252.51-296.32 kJ (mol-O)$^{-1}$ and 126.95-168.85 J (mol-O)$^{-1}$ K^{-1}, respectively.

Conclusions

In summary, we reported a new A-site high-entropy HPEOs based on LS21_Mn as the parent perovskite-type oxide for solar-driven thermochemical water splitting. Notably, $(La_{1/6}Pr_{1/6}Nd_{1/6}Gd_{1/6}Sr_{1/6}Ba_{1/6})MnO_3$ (LPNGSB_Mn) shows an excellent balance between fast kinetics and suitable thermodynamics as well as extraordinary phase stability during the redox reaction. It exhibits moderate enthalpy (ranging between 252.51 and 296.32 kJ (mol-O)$^{-1}$) and entropy (ranging between 126.95 and 168.85 J (mol-O)$^{-1}$ K^{-1}) of reduction. These traits of LPNGSB_Mn enable a maximum hydrogen production of ~77.5 mmol mol_{oxide}^{-1} within a short 1-hour duration under optimized STCH conditions. We further showed that Mn is the only redox-active element in this HEPO. LPNGSB_Mn shows excellent phase stability and cycling durability over 50 cycles. This STCH technology can be also extended to thermochemical seawater splitting, eliminating the strict requirements of high-purity water. This study opens new avenues for screening redox materials for STCH and other possible chemical looping reactions. We suggest future studies focusing on testing this high entropy oxide in a reticulated porous ceramic structure for practical applications and exploring in-depth mechanisms.

Experimental section

3.1 Materials Synthesis

All perovskite-type oxide powders were synthesized using a solid-state method. The chemical precursors were used without further purification. Stoichiometric amounts of La_2O_3 (Alfa Aesar, 99.99%), Pr_6O_{11} (Alfa Aesar, 99.99%), Nd_2O_3 (Sigma Aldrich, 99.99%), Gd_2O_3 (Alfa Aesar, 99.99%), $SrCO_3$ (Alfa Aesar, 99.99%), $BaCO_3$ (Sigma Aldrich, 99.98%) and MnO_2 (Alfa Aesar 99.9%) were placed in a poly(methyl methacrylate) high-energy ball mill (HEBM) vial with endcaps and millings balls made of tungsten carbide, and dry milled for 100 min (SPEX 8000D, SPEX SamplePrep, USA). The mixed powder was heated from room temperature (RT) to 1300 °C with a heating rate of 5 °C min^{-1} and annealed in air at 1300 °C for 10 hours. Subsequently, the annealed powder was cooled to RT at a rate of 5 °C min^{-1}. After that, the synthesized powder was ground with a pestle and mortar to achieve uniform mixing and prevent local non-uniformities. Then, the powder was further annealed at 1400 °C with a heating/cooling rate of 5 °C min^{-1} for 10 hours to enhance the homogeneity of the final product.

3.2 Phase Characterization

The phases were confirmed by X-ray diffraction (XRD) using a powder diffractometer (Rigaku Miniflex) at 30kV and 15mA, with Cu K_α radiation. All XRD data were collected with a step size of 0.02° and a scan rate of 2° min^{-1}. The crystal structures of powders and specific crystallographic parameters were analysed by Rietveld refinement (Crystallography data analysis software: GSAS-II). The crystallographic information file (CIF) of $La_{0.65}Sr_{0.35}MnO_3$ ($R\bar{3}c$) from the Inorganic Crystal Structure Database (#54-1195) was used as an initial structure.

3.3 Pair Distribution Function

Pair distribution function (PDF) $G(r)$ analysis was obtained via neutron total scattering at Nanoscale-Ordered Materials Diffractometer (NOMAD BL-1B) at the Spallation Neutron Source (SNS) of the Oak Ridge National Laboratory (ORNL). All perovskite powder specimens (around 0.6 g) were loaded into quartz capillaries (Hampton Research, HR6-150, 2 mm diameter and 8 cm length). The total scattering experiments were carried out at 290 K for a total accelerator proton charge of 8 C, corresponding to about 92 min acquisition time at the full power. To produce the total scattering function $S(Q)$, the background was subtracted for the data from six detector banks and the data were normalized to the intensity of vanadium. This function was Fourier-transformed with a sliding Q_{max} to obtain the neutron weighted pair distribution functions, $G(r) = r[g(r)-1]$. The shortest distance correlations were transformed with a Q_{max} =31.4 $Å^{-1}$. The momentum transfer, Q, is given as $Q=\frac{4\pi\sin\theta}{\lambda}$, where θ and λ are the scattering angle and the neutron wavelength, respectively. The analysis of PDF data was done with small-box modeling by the PDFgui software. Rhombohedral ($R\bar{3}c$) structure was used to model the data. The refined parameters include lattice parameters (a and c), scale factor, linear correlated motion factor (Delta 2 in PDFgui), isotropic atomic displacement parameters (ADP) for A-, B- and O sites, and the number of oxygen vacancies. Multiple elements occupying A or B site were refined with the same XYZ position and ADP.

3.4 Temperature Programmed Reduction Experiment

Temperature programmed reduction (TPR) characterization was conducted using a simultaneous thermal analyzer (STA 449 F3 Jupiter, NETZSCH Germany). Around 30 mg of powder sample was heated up to 1350 °C with a heating rate of 30 °C min^{-1} and held isothermally for 45 min in ultrahigh-purity (UHP) Ar atmosphere. Subsequently, the sample was cooled down to 1100 °C with a cooling rate of 30 °C min^{-1}. Then, 21% O_2 mixed with 79% Ar was introduced to oxidize the sample. A blank crucible was tested to calibrate the mass loss curve of samples. The extent of reduction ($\Delta\delta$) was then calculated by measuring the mass change of the sample,[89] which should remain constant to confirm complete oxidation under these conditions. The initial cycle usually displayed activation behaviours because of surface adsorption. Thus, the stabilized cycle 2 for all LPNGSB_Mn samples was reported for comparison.

3.5 Electron Paramagnetic Resonance (EPR) Spectroscopy

EPR spectra were recorded using a Bruker ELEXSYS spectrometer (Bruker BioSciences, Billerica, MA, USA) operating at X-band with a 100 kHz modulation frequency as described previously.[90, 91] Solid/powder samples were loaded directly in to an EPR quartz tube (O.D 4 mm). The quartz tube was positioned inside the resonator/cavity and the sample was adjusted to the middle of the resonator. EPR spectra were recorded at room temperature. Data acquisition was performed using Bruker Xepr software. The following settings were used: microwave frequency, 9.86 GHz; microwave power, 15 mW; modulation amplitude, 4.91 G; modulation frequency, 100 kHz; receiver gain, 60 dB; conversion time, 29.3 ms; sweep time, 120 s; number of scans, 1. Data processing was performed using GraphPad Prism 10 program.

3.6 Scanning Transmission Electron Microscopy (STEM)

Electron transparent specimens were prepared using a Helios Nanolab 660 dual beam focused ion beam (FIB)/scanning electron microscope (Thermo Fisher Scientific). The procedure for preparing the FIB TEM lamella, including using a protective Pt coating on the surface of the samples. Bulk material removal and thinning were performed at 30 kV. The final thinning was performed at 5 kV to prevent further incidental Ga beam damage and remove previously damaged. STEM analysis was performed with a probe-corrected Titan Themis Z electron microscope operated at 300 kV (Thermo Fisher Scientific). The TEM is equipped with a monochromator (0.14 eV fwhm ZLP @ 300 kV), large-solid angle SDD EDX detector (Super

X, solid angle ≈ 0.7 sr), and Quantum 969 EELS spectrometer (Gatan, Inc.), which has both a conventional CCD and a direct-electron CMOS K2 sensor for electron counting mode EELS analysis.

3.7 In-situ Scanning Transmission Electron Microscopy (STEM) Combined with Electron Energy Loss Spectroscopy (EELS)

In situ heating was performed with a Gatan double-tilt model 652 heating holder. The sample was heated in a microscope vacuum (approximately 5.6×10^{-8} Torr; therefore, less than 4×10^{-8} bar O_2) to the desired temperature at a ramp rate of approximately 10 °C min^{-1} and then held for approximately 15 min to allow time for drift to settle and the sample to equilibrate. EELS spectra of LPNGSB_Mn samples were collected at 25, 250, 400, 500, 600, and 700 °C. EELS spectra were collected in identical sample locations at a given temperature before and after the sample was heated to the next target temperature. For monochromated EELS, the convergence angle was approximately 25 mrad. The collection angle was approximately 35 mrad, and typical beam currents were 100−200 pA. To avoid a strong contribution from the electron beam during heating, the beam was quickly scanned over an area of interest during spectrum acquisition so that the electron dose was spread out over an area and not focused on one point. Additionally, EELS spectra were collected using Digital Micrograph's "time series" mode. Individual EELS spectra were collected with a 20−50 ms integration time while the beam scanned over a selected region of the sample, and then 5000−8000 spectra were summed up to increase signal-to-noise. The K2 sensor was used for these measurements. The regions of the sample that were selected were always within a single phase and compositionally uniform region of the sample.

3.8 X-ray Photoelectron Spectroscopy

XPS measurements were performed using a PHI VersaProbe 5000 Scanning X-Ray Photoelectron Spectrometer (ULVAC-PHI, Inc.) at room temperature and under a vacuum better than $1e^{-6}$ Pascal. All measurements were performed using a focused Al K-Alpha X-ray source with a photon energy of 1486 eV and power of 25 W, along with an X-ray spot size of 100 µm. To correct sample charging effects, a primary electron neutralizer and a secondary Ar^+ ion neutralizer were used. The take-off angle of the photoelectron was set at 45 degrees. Compositional survey scans were obtained using a pass energy of 117.4 eV and an energy step of 0.5 eV. High-resolution detailed scans for each element were acquired using a pass energy of 23.5 eV and an energy step of 0.1 eV. The C 1s peak signal at 284.8 eV served as a reference for calibrating the binding energies.

3.9 Thermochemical Water Splitting Measurements

LS21_Mn and LPNGSB_Mn compositions were also tested in Sandia National Laboratories' (SNL) stagnation flow reactor (SFR) equipped with a 500 W near-IR continuous-wave laser for rapid sample heating. A mass spectrometer was positioned downstream of the SFR for gas analysis. All systems were operated under a sub-ambient pressure of 75 Torr. For calibration of the mass spectrometer, aliquots of oxygen and hydrogen were utilized. These were regulated using mass flow controllers and sourced from verified gas mixture standards, specifically 25% oxygen in argon (Ar) and 5% hydrogen in argon. Approximately 100 mg of powder samples were evenly distributed on a shallow platinum crucible supported by a zirconia fibreboard holder to form a thin bed. The reactor was then brought to the oxidation temperature (T_{ox}) under an ultra-high purity argon atmosphere. The samples were reduced by laser-heating from T_{ox} to the reduction temperature (T_{red}) at a rate of 10 °C s^{-1}, then returned to T_{ox} after a fixed reduction duration. To initiate the reoxidation process, a gas flow containing 40 vol% water vapour in Ar was introduced. The total quantities of released oxygen and produced hydrogen were determined by integrating the signals from the mass spectrometer, which were adjusted for baseline corrections, across the entire period of gas evolution. Further details about the testing conditions have been published elsewhere.[63, 64] **Table S4** shows the detailed protocols. The STCH cycling experiments were conducted by a homemade flow reactor. The powder (approximately 0.1 g) was loaded into the middle of an alumina tube (AdValue Technology, OD 1/4'' × ID 3/16'' × L 24'') and placed horizontally near the thermocouple within a programmed heating and cooling electric furnace. The powder was uniformly dispersed in the tube to ensure sufficient gas-solid contact. There was some space over the powder to prevent a sudden pressure drop and avoid powder blowing off. N_2 (Matheson UHP) was used as a carrier gas, and a mass flow controller (Alicat Scientific) was used to control the flow rate. The steam (40 vol% H_2O) was generated by a water evaporator (Fuel Cell Technologies, Inc. Humidity bottle). N_2 was used to balance the steam and create the desired oxidation conditions. The outlet was connected to a cold trap, which condensed steam into water. The total amount of hydrogen produced was collected using the Restek Sample Gas Bag (10 L) for a given duration. Then, the H_2 product concentration in the gas bag was detected using the gas chromatography (GC, Shimadzu GC-2014) with a thermal conductivity detector (TCD) which was calibrated with a series of standard H_2 gases (GASCO, Cal Gas Direct Inc.) with different known and certified concentrations balanced by N_2. The direct water thermolysis part at different temperatures was subtracted from the total H_2 production.

4.0 Measurements of Thermodynamic Properties

The thermodynamic properties (the enthalpy and entropy of reduction) of LPNGSB_Mn and LS21_Mn were measured up to 1450 °C under different P_{O_2} conditions spanning from $10^{-0.58}$ to $10^{-4.59}$ atm. About 500 mg of sample was used in the TGA measurements, which was tested using a NETZSCH STA 449 F1. Oxygen partial pressure was controlled by mixing oxygen, argon, and pre-mixed 1100 ppm O_2 in argon and measured on the exhaust side of the instrument using a Zirox ZR5 oxygen sensor. Corrections for buoyancy were performed

using a crucible filled with coarse alumina powder to approximate the same volume of powder as measured samples.

Author Contributions

C.L. and D.Z. contributed equally to this work. C.L., D.Z. and W.L. (Wei Li) designed the experiments and methodology. C.L. contributed to STCH materials screening and cycling stability tests. D.Z. synthesized materials and conducted most material characterizations. C.L. and D.Z. analysed the data and prepared the figures and plots. W.L. (Wei Li) conceived the work and sample composition. J.A.T, J.D.S., and A.L.C. contributed the STEM, EELS, and a part of SEM characterizations. K.A.K. and A.H.M. performed the STCH measurements with the reactor at Sandia National Laboratories. S.R.B., A.I.S. P.A.S. and E.N.C. contributed to the TGA measurements under different temperatures and P_{O_2} for acquiring enthalpy and entropy of reduction. M.V. and V.V.K. conducted the EPR measurements and analysed the EPR data. J.C.N. contributed to neutron total scattering and PDF characterizations. Q.W. (Qiang Wang) assisted in Raman and XPS characterizations. W.L. (Wenyuan Li) and H.T. assisted in the ECR characterization. J.Y. assisted in the synthesis and material characterization. Q.W. (Qingsong Wang) and Q.L. assisted in investigating the redox process. H.N.N.T., B.R., J.H. and A.M.D. assisted in STCH testing. H.A.D.S. contributed to the sample synthesis and assisted in STCH testing. L.M., Y.W. and G.C. contributed to the STCH reactor construction. X.L. (Xuemei Li) and N.A.T.T. assisted in SEM characterization. C.L. D.Z. and W.L. (Wei Li) wrote the original draft. All authors reviewed and commented the manuscript. Project administration, funding acquisition, and supervision, W.L. (Wei Li), J.L. and X.L. (Xingbo Liu).

Conflicts of interest

The authors declare no competing financial interest.

Acknowledgements

This work is supported by the U.S. Department of Energy (DOE), Office of Energy Efficiency and Renewable Energy (EERE), under the Agreement Number DE-EE0008839, managed by the Hydrogen and Fuel Cell Technologies Office in the Fiscal Year 2019 H_2@SCALE program.

Sandia National Laboratories is a multi-mission laboratory managed and operated by National Technology and Engineering Solutions of Sandia, LLC., a wholly owned subsidiary of Honeywell International, Inc., for the U.S. Department of Energy's National Nuclear Security Administration under contract DE-NA0003525. This article has been authored by an employee of National Technology & Engineering Solutions of Sandia, LLC under Contract No. DE-NA0003525 with the U.S. Department of Energy (DOE). The employee owns all right, title and interest in and to the article and is solely responsible for its contents. The United States Government retains and the publisher, by accepting the article for publication, acknowledges that the United States Government retains a non-exclusive, paid-up, irrevocable, world-wide license to publish or reproduce the published form of this article or allow others to do so, for United States Government purposes. The DOE will provide public access to these results of federally sponsored research in accordance with the DOE Public Access Plan. This paper describes objective technical results and analysis. Any subjective views or opinions that might be expressed in the paper do not necessarily represent the views of the U.S. Department of Energy or the United States Government.

The Alliance for Sustainable Energy, LLC, operates and manages the National Renewable Energy Laboratory (NREL) for DOE under contract no. DE-AC36-08GO28308. A part of this research used resources at the Spallation Neutron Source (SNS), a Department of Energy Office of Science User Facility operated by the Oak Ridge National Laboratory. The use of the WVU Shared Research Facilities is acknowledged. We thank Dr. Xin Qian at Northwestern University for the technical discussion of direct water thermolysis, Dr. J. Madhusudhan Naik at University of Zurich for the technical discussion of thermodynamics and configurational entropy, and Dr. Yue Qi and Boyuan Xu at Brown University for the theoretical computation discussion.

Notes and references

1. J. D. Holladay, J. Hu, D. L. King and Y. Wang, *Catal Today*, 2009, **139**, 244-260.
2. W. Lubitz and W. Tumas, *Chem Rev*, 2007, **107**, 3900-3903.
3. Z. X. Cai, Z. L. Wang, Y. J. Xia, H. Lim, W. Zhou, A. Taniguchi, M. Ohtani, K. Kobiro, T. Fujita and Y. Yamauchi, *Angew Chem Int Ed*, 2021, **60**, 4747-4755.
4. M. Luo, J. T. Yang, X. G. Li, M. Eguchi, Y. Yamauchi and Z. L. Wang, *Chem Sci*, 2023, **14**, 3400-3414.
5. Z. Y. Zhang, H. Tian, L. Bian, S. Z. Liu, Y. Liu and Z. L. Wang, *J. Energy Chem.*, 2023, **83**, 90-97.
6. A. Onigbajumo, P. Swarnkar, G. Will, T. Sundararajan, A. Taghipour, S. Couperthwaite, T. Steinberg and T. Rainey, *J. Clean Prod.*, 2022, **371**, 133303.
7. A. Bayon, A. de la Calle, E. B. Stechel and C. Muhich, *Energy Technol.*, 2022, **10**, 2100222.
8. C. L. Muhich, B. D. Ehrhart, V. A. Witte, S. L. Miller, E. N. Coker, C. B. Musgrave and A. W. Weimer, *Energy Environ. Sci.*, 2015, **8**, 3687-3699.
9. J. E. Miller, A. H. McDaniel and M. D. Allendorf, *Adv. Energy Mater.*, 2014, **4**, 1300469.
10. L. Zhou, X. Li, Q. Li, A. Kalu, C. Liu, X. Liu and W. Li, *ACS Catal*, 2023, **13**, 15087-15106.
11. A. Steinfeld, *Sol Energy*, 2005, **78**, 603-615.
12. Z. P. Chen, Q. Q. Jiang, F. Cheng, J. H. Tong, M. Yang, Z. X. Jiang and C. Li, *J. Mater. Chem. A*, 2019, **7**, 6099-6112.
13. S. Abanades, P. Charvin, F. Lemont and G. Flamant, *Int. J. Hydrog. Energy*, 2008, **33**, 6021-6030.
14. P. G. Loutzenhiser, A. Meier and A. Steinfeld, *Materials*, 2010, **3**, 4922-4938.

15. I. E. Yigiter and B. Piskin, *Jom*, 2022, **74**, 4682-4694.
16. S. Abanades and G. Flamant, *Sol Energy*, 2006, **80**, 1611-1623.
17. W. C. Chueh and S. M. Haile, *Chemsuschem*, 2009, **2**, 735-739.
18. H. Kaneko, T. Miura, H. Ishihara, S. Taku, T. Yokoyama, H. Nakajima and Y. Tamaura, *Energy*, 2007, **32**, 656-663.
19. P. Singh and M. S. Hegde, *Chem Mater*, 2010, **22**, 762-768.
20. A. H. Bork, M. Kubicek, M. Struzik and J. L. M. Rupp, *J. Mater. Chem. A*, 2015, **3**, 15546-15557.
21. M. Orfila, M. Linares, R. Molina, J. A. Botas, R. Sanz and J. Marugan, *Int J Hydrogen Energ*, 2016, **41**, 19329-19338.
22. L. L. Wang, M. Al-Mamun, Y. L. Zhong, L. X. Jiang, P. R. Liu, Y. Wang, H. G. Yang and H. J. Zhao, *Sustain. Energ. Fuels*, 2017, **1**, 1013-1017.
23. X. Qian, J. G. He, E. Mastronardo, B. Baldassarri, W. Z. Yuan, C. Wolverton and S. M. Haile, *Matter*, 2021, **4**, 688-708.
24. M. Ezbiri, M. Takacs, D. Theiler, R. Michalsky and A. Steinfeld, *J. Mater. Chem. A*, 2017, **5**, 4172-4182.
25. D. B. Miracle, J. D. Miller, O. N. Senkov, C. Woodward, M. D. Uchic and J. Tiley, *Entropy*, 2014, **16**, 494-525.
26. S. Akrami, P. Edalati, M. Fuji and K. Edalati, *Mater Sci Eng R*, 2021, **146**, 100644.
27. C. Oses, C. Toher and S. Curtarolo, *Nat. Rev. Mater.*, 2020, **5**, 295-309.
28. A. J. Wright and J. Luo, *J Mater Sci*, 2020, **55**, 9812-9827.
29. S. C. Jiang, T. Hu, J. Gild, N. X. Zhou, J. Y. Nie, M. D. Qin, T. Harrington, K. Vecchio and J. Luo, *Scripta Mater*, 2018, **142**, 116-120.
30. A. Amiri and R. Shahbazian-Yassar, *J. Mater. Chem. A*, 2021, **9**, 782-823.
31. Z. Q. Li, B. Guan, F. Xia, J. Y. Nie, W. Y. Li, L. Ma, W. Li, L. F. Zhou, Y. Wang, H. C. Tian, J. Luo, Y. Chen, M. Frost, K. An and X. B. Liu, *Acs Appl Mater Interfaces*, 2022, **14**, 24363-24373.
32. X. Yang, R. K. Guo, R. Cai, Y. J. Ouyang, P. P. Yang and J. F. Xiao, *Int J Hydrogen Energ*, 2022, **47**, 13561-13578.
33. D. W. Zhang, J. Park, B. Y. Xu, C. J. Liu, W. Li, X. B. Liu, Y. Qi and J. Luo, *Dalton Trans*, 2023, **52**, 1082-1088.
34. A. Le Gal, M. Valles, A. Julbe and S. Abanades, *Catalysts*, 2022, **12**, 1116.
35. S. Zhai, J. Rojas, N. Ahlborg, K. Lim, M. F. Toney, H. Y. Jin, W. C. Chueh and A. Majumdar, *Energy Environ. Sci.*, 2018, **11**, 2172-2178.
36. M. Biesuz, L. Spiridigliozzi, G. Dell'Agli, M. Bortolotti and V. M. Sglavo, *J Mater Sci*, 2018, **53**, 8074-8085.
37. R. Djenadic, A. Sarkar, O. Clemens, C. Loho, M. Botros, V. S. K. Chakravadhanula, C. Kubel, S. S. Bhattacharya, A. S. Gandhif and H. Hahn, *Mater. Res. Lett.*, 2017, **5**, 102-109.
38. A. Sarkar, R. Djenadic, D. Wang, C. Hein, R. Kautenburger, O. Clemens and H. Hahn, *J Eur Ceram Soc*, 2018, **38**, 2318-2327.
39. Y. B. Gao, Y. P. Mao, Z. L. Song, X. Q. Zhao, J. Sun, W. L. Wang, G. F. Chen and S. Y. Chen, *Appl. Energy*, 2020, **279**, 115777.
40. A. J. Wright, Q. Y. Wang, C. Y. Huang, A. Nieto, R. K. Chen and J. Luo, *J Eur Ceram Soc*, 2020, **40**, 2120-2129.
41. D. W. Zhang, H. A. De Santiago, B. Y. Xu, C. J. Liu, J. A. Trindell, W. Li, J. Park, M. A. Rodriguez, E. N. Coker, J. D. Sugar, A. H. McDaniel, S. Lany, L. Ma, Y. Wang, G. Collins, H. C. Tian, W. Y. Li, Y. Qi, X. B. Liu and J. Luo, *Chem Mater*, 2023, **35**, 1901-1915.
42. Y. J. Han, M. Tian, C. J. Wang, T. Zong and X. D. Wang, *Appl Catal B-environ*, 2023, **339**, 123096.
43. Y. B. Gao, M. M. Zhang, Y. P. Mao, H. Cao, S. J. Zhang, W. L. Wang, C. G. Sun, Z. L. Song, J. Sun and X. Q. Zhao, *Energ Convers Manag*, 2022, **252**, 115125.
44. D. R. Munazat, B. Kurniawan and Iop, *J Phys Conf Ser* 2019, **1170**, 012051.
45. M. D. Sanders, A. M. Bergeson-Keller, E. N. Coker and R. P. O'Hayre, *Front. Energy Res.*, 2022, **10**, 856943.
46. C. Zhao, C. Li, H. Liu, Q. Qiu, F. S. Geng, M. Shen, W. Tong, J. X. Li and B. W. Hu, *J Am Chem Soc*, 2021, **143**, 18652-18664.
47. R. A. Eichel, *Phys Chem Chem Phys*, 2011, **13**, 368-384.
48. D. Cordischi, M. Faticanti, G. Minelli, M. Occhiuzzi and P. Porta, *Phys Chem Chem Phys*, 2003, **5**, 1467-1473.
49. V. A. Ivanshin, J. Deisenhofer, H. A. K. von Nidda, A. Loidl, A. A. Mukhin, A. M. Balbashov and M. V. Eremin, *Phys Rev B*, 2000, **61**, 6213-6219.
50. M. T. Causa, M. Tovar, A. Caneiro, F. Prado, G. Ibanez, C. A. Ramos, A. Butera, B. Alascio, X. Obradors, S. Pinol, F. Rivadulla, C. Vazquez-Vazquez, M. A. Lopez-Quintela, J. Rivas, Y. Tokura and S. B. Oseroff, *Phys Rev B*, 1998, **58**, 3233-3239.
51. Y. Zhao, J. P. Zhu, H. L. Wang, Z. Ma, L. H. Gao, Y. B. Liu, Y. Liu, Y. C. Shu and J. L. He, *Ceram Int*, 2021, **47**, 5549-5558.
52. Z. Li, W. J. Yang, L. B. Xie, Y. Li, Y. Liu, Y. Sun, Y. F. Bu, X. Y. Mi, S. H. Zhan and W. P. Hu, *Appl Surf Sci*, 2021, **549**, 149278.
53. Z. Wei, M. Zhao, Z. Yang, X. Duan, G. Jiang, G. Li, F. Zhang and Z. Hao, *Proc Natl Acad Sci U S A*, 2023, **120**, e2217148120.
54. M. K. Dalai, R. Kundu, P. Pal, M. Bhanja, B. R. Sekhar and C. Martin, *J Alloy Compd*, 2011, **509**, 7674-7676.
55. M. C. Biesinger, B. P. Payne, A. P. Grosvenor, L. W. M. Lau, A. R. Gerson and R. S. Smart, *Appl Surf Sci*, 2011, **257**, 2717-2730.
56. Y. F. Li, W. Q. Zhang, Y. Zheng, J. Chen, B. Yu, Y. Chen and M. L. Liu, *Chem Soc Rev*, 2017, **46**, 6345-6378.
57. B. Koo, K. Kim, J. K. Kim, H. Kwon, J. W. Han and W. Jung, *Joule*, 2018, **2**, 1476-1499.
58. Q. Q. Jiang, Z. P. Chen, J. H. Tong, M. Yang, Z. X. Jiang and C. Li, *Chem Commun*, 2017, **53**, 1188-1191.
59. Z. P. Chen, Q. Q. Jiang, J. H. Tong, M. Yang, Z. X. Jiang and C. Li, *Sol Energy*, 2017, **144**, 643-659.
60. C. L. Muhich, K. C. Weston, D. Arifin, A. H. McDaniel, C. B. Musgrave and A. W. Weimer, *Ind Eng Chem Res*, 2015, **54**, 4113-4122.
61. T. C. Davenport, M. Kemei, M. J. Ignatowich and S. M. Haile, *Int J Hydrogen Energ*, 2017, **42**, 16932-16945.
62. J. R. Scheffe, A. H. McDaniel, M. D. Allendorf and A. W. Weimer, *Energy Environ. Sci.*, 2013, **6**, 963-973.
63. D. R. Barcellos, M. D. Sanders, J. H. Tong, A. H. McDaniel and R. P. O'Hayre, *Energy Environ. Sci.*, 2018, **11**, 3256-3265.
64. R. B. Wexler, G. S. Gautam, R. T. Bell, S. Shulda, N. A. Strange, J. A. Trindell, J. D. Sugar, E. Nygren, S. Sainio, A. H. McDaniel, D. Ginley, E. A. Carter and E. B. Stechel, *Energy Environ. Sci.*, 2023, **16**, 2550-2560.
65. L. L. Wang, M. Al-Mamun, P. R. Liu, Y. L. Zhong, Y. Wang, H. G. Yang and H. J. Zhao, *Acta Metall. Sin.-Engl. Lett.*, 2018, **31**, 431-439.
66. W. Li, H. C. Tian, L. Ma, Y. Wang, X. B. Liu and X. F. Gao,

Mater. Adv., 2022, **3**, 5598-5644.
67. W. M. Tong, M. Forster, F. Dionigi, S. Dresp, R. S. Erami, P. Strasser, A. J. Cowan and P. Farras, *Nature Energy*, 2020, **5**, 367-377.
68. Y. Yu, C. Y. Cao, W. Li, P. Li, J. Qu and W. G. Song, *Nano Res.*, 2012, **5**, 434-442.
69. W. Li, X. F. Gao, D. H. Xiong, F. Wei, W. G. Song, J. Y. Xu and L. F. Liu, *Adv. Energy Mater.*, 2017, **7**, 1602579.
70. Y. Wang, W. Y. Li, L. Ma, W. Li and X. B. Liu, *J Mater Sci Technol*, 2020, **55**, 35-55.
71. W. Li, D. H. Xiong, X. F. Gao, W. G. Song, F. Xia and L. F. Liu, *Catal Today*, 2017, **287**, 122-129.
72. Y. P. Cao, M. J. Gadre, A. T. Ngo, S. B. Adler and D. D. Morgan, *Nat Commun*, 2019, **10**, 1346.
73. H. Qi, Y. L. Lee, T. Yang, W. Y. Li, W. Li, L. Ma, S. S. Hu, Y. H. Duan, G. A. Hackett and X. B. Liu, *ACS Catal*, 2020, **10**, 5567-5578.
74. T. Runka and M. Berkowski, *J Mater Sci*, 2012, **47**, 5393-5401.
75. T. Scherban, R. Villeneuve, L. Abello and G. Lucazeau, *J Raman Spectrosc*, 1993, **24**, 805-814.
76. M. C. Weber, J. Kreisel, P. A. Thomas, M. Newton, K. Sardar and R. I. Walton, *Phys Rev B*, 2012, **85**, 054303.
77. M. N. Iliev and M. V. Abrashev, *J Raman Spectrosc*, 2001, **32**, 805-811.
78. H. C. Gupta, M. K. Singh and L. M. Tiwari, *J Raman Spectrosc*, 2002, **33**, 67-70.
79. N. Dilawar, U. Chandra, G. Parthasarathy and A. K. Bandyopadhyay, *J Raman Spectrosc*, 2008, **39**, 1765-1771.
80. X. Yu, C. W. Hu, P. X. Ji, Y. M. Ren, H. Y. Zhao, G. Liu, R. Xu, X. D. Zhu, Z. Q. Li, Y. Q. Ma and L. Ma, *Appl Catal B-environ*, 2022, **310**, 121301.
81. K. J. Warren, J. T. Tran and A. W. Weimer, *Energy Environ. Sci.*, 2022, **15**, 806-821.
82. J. Park, B. Y. Xu, J. Pan, D. W. Zhang, S. Lany, X. B. Liu, J. Luo and Y. Qi, *npj Comput. Mater.*, 2023, **9**, 29.
83. X. Qian, S. M. Haile, T. C. Davenport and E. Mastronardo, *J Am Ceram Soc*, 2022, **105**, 4375-4386.
84. R. J. Panlener, R. N. Blumenthal and J. E. Garnier, *J Phys Chem Solids*, 1975, **36**, 1213-1222.
85. Y. Hao, C. K. Yang and S. M. Haile, *Chem Mater*, 2014, **26**, 6073-6082.
86. J. Mizusaki, Y. Mima, S. Yamauchi, K. Fueki and H. Tagawa, *J Solid State Chem*, 1989, **80**, 102-111.
87. M. J. Ignatowich, A. H. Bork, T. C. Davenport, J. L. M. Rupp, C. K. Yang, Y. Yamazaki and S. M. Haile, *MRS Commun.*, 2017, **7**, 873-878.
88. S. R. Bishop, D. W. Zhang, C. J. Liu, W. Li, P. A. Salinas, A. I. Smith, E. N. Coker, H. A. De Santiago, X. B. Liu, A. H. McDaniel and J. Luo, *ECS Transactions*, 2023, **111**, 1135.
89. A. Riaz, T. Tsuzuki, F. Kremer, S. Sattayaporn, M. U. Ali, W. Lipinski and A. Lowe, *ACS Catal*, 2020, **10**, 8263-8276.
90. X. J. Chen, W. Li, Y. B. Xu, Z. P. Zeng, H. C. Tian, M. Velayutham, W. Y. Shi, W. Y. Li, C. M. Wang, D. Reed, V. V. Khramtsov, X. L. Li and X. B. Liu, *Nano Energy*, 2020, **75**, 104869.
91. N. Majumder, W. T. Goldsmith, V. K. Kodali, M. Velayutham, S. A. Friend, V. V. Khramtsov, T. R. Nurkiewicz, A. Erdely, P. C. Zeidler-Erdely, V. Castranova, J. R. Harkema, E. E. Kelley and S. Hussain, *Redox Biol.*, 2021, **46**, 102092.

